

Supplemental Peak Filters for Advanced Disturbance Rejection on a High Precision Endeffector for Robot-based Inline Metrology

Ernst Csencsics*, Markus Thier*, Shingo Ito, Georg Schitter, *Senior Member, IEEE*

Abstract—This paper presents a measurement platform (MP) as high precision endeffector of a robot with a tailored disturbance rejection scheme, in order to enable high-resolution measurements directly in a production line. The MP is installed on a gantry robot for in-plane positioning and has an electromagnetic actuator for vertically positioning its mover. It can mount a compact measurement tool for high precision topography measurements, which are typically sensitive to external vibrations, introducing relative motion between the measurement tool and the sample. To compensate these vibrations, the MP mover vertically tracks the sample by feedback control, maintaining a constant distance between sample and measurement tool. In order to reject broad-band floor vibrations as well as narrow-band vibrations, revealed by the analysis and introduced by the robots servo control, the designed high-bandwidth PID-based controller is supplemented by peak filters tailored to the narrow-band vibration components. A method for designing these peak filters depending on the location of the narrow-band disturbance relative to the crossover frequency is presented. The resulting controller enables a tracking error as small as 15 nm(rms), which is 50% smaller than the error without the peak filters, demonstrating the effectiveness of the MP in enabling high resolution inline measurements.

Index Terms—Precision Engineering, Disturbance rejection, Motion control, Inline metrology.

I. INTRODUCTION

INLINE metrology enhances the quality control of industrial production processes by evaluating the product quality directly in the production line and adjusting the production settings accordingly [1]. Dependent on the production process, e.g. coating [2] or grinding [3], various surface properties of a good, such as topography or roughness, are of interest, which they are typically evaluated by high-resolution measurement instruments, such as atomic force microscopes (AFMs) [4], [5] or scanning optical 3D sensors [6]. These instruments, however, usually require means for vibration isolation because floor vibrations, caused by operators and manufacturing machines on the work floor, impair high-resolution measurements [4], [7].

Commonly used vibration isolators are equipped with a tabletop mounting for measurement instruments. The tabletop is suspended by supports that decouple it passively or actively from the floor for vibration isolation [8]. When such

*) Authors contributed equally to the publication. The authors are with Christian Doppler Laboratory for Precision Engineering for Automated In-Line Metrology, Automation and Control Institute (ACIN), TU Wien, Gusshausstrasse 27-29, 1040 Vienna, Austria e-mail: csencsics@acin.tuwien.ac.at.

a vibration isolator is used for product inspection, samples from the production line need to be transferred to a laboratory environment, which clearly prevents a 100% quality control or significantly impairs the throughput. Additionally, vibrations at low frequencies cannot be isolated due to the supports' stiffness and the noise of vibration sensors in passive [8] as well as active vibration isolators [9].

The flexibility to quickly locate a measurement tool over various regions of interest on a produced good directly in a production line can be provided by employing industrial robots. They extend the range of the measurement tool [10] and enable fully automatic measurement operations [11]. However, the typical positioning accuracy and resolution of nowadays industrial robots is in the range of several tens of micrometers [12]. The limited positioning accuracy, similar as environmental vibrations, causes relative motion between a robot-mounted measurement tool during the measurement process and leads to motion blur in the measurement results in all degrees of freedom. This entails corrupted measurements, making robots themselves insufficient for conducting measurements with high precision measurement tools on the micrometer scale and below.

In order to overcome the aforementioned shortcomings, active sample-tracking vibration isolation [13] has been proposed to enable high precision inline measurements [14]. While sample-tracking vibration isolation itself has been successfully demonstrated [13], [14] and already been integrated into a tabletop AFM [15], it remains unclear if it can also be used to improve the positioning precision of a robot-based inline metrology system. One major concern is that the mechanical loop from the measurement tool to the sample is significantly enlarged, such that the measurement system may become even more sensitive to floor vibrations [4]. Another concern is that vibrations induced by the operation of the robot itself, impair the the positioning precision of the system.

The contribution of this paper is (i) the design and analysis of a metrology platform (MP) as endeffector for robot-based high precision inline measurements, capable of carrying a compact measurement tool and compensating external vibrations in vertical direction, and (ii) a method for tailoring supplemental peak filters to the noise properties of the used robot, extending the feedback controller for improved active sample surface tracking. The positioning systems, comprising a gantry robot and the MP, is designed in Section II, followed by an analysis of the dynamics and vibration characteristics in Section III. Based on the analysis, the motion controller

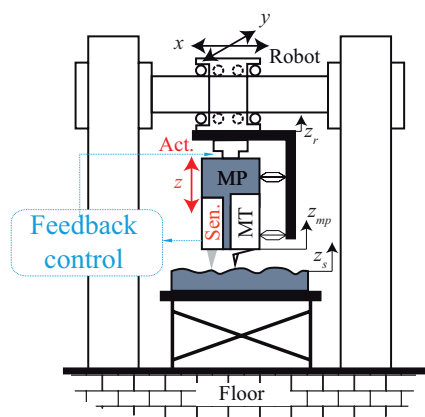


Fig. 1. Vibration compensation concept with metrology platform (MP). The relative distance between the measurement tool (MT) and the sample is measured by a tracking sensor and kept constant by feedback control via a vertical z actuator. Vibrations from the robot z_r and the sample z_s are canceled and not influencing the measurement.

is designed and tailored to the vibrational characteristic of the robot via the proposed design method in Section IV. Section V experimentally evaluates the tracking performance of the positioning system with the tailored controller. Section VI concludes the paper.

II. SYSTEM DESIGN

The entire positioning system comprises the MP for vertical positioning of the measurement tool in constant proximity above the sample and a gantry robot for lateral positioning of the entire MP in the working space of the robot. Figure 1 shows an overview schematic of the developed system design. The MP carries the measurement tool and includes a vertical actuator and a tracking sensor to measure the distance between measurement tool and sample [16]. The sensor signal is used for feedback control, such that the distance between the measurement tool and the sample is kept constant by actively controlling the MP mover position. The MP thus tracks the sample to isolate and reject vibrations from the robot and the sample to enable vibration-free high resolution measurements [17]. As illustrated, the MP is installed on the carriage of the robot in order to place it at arbitrary measurement locations on the sample. When the MP reaches a targeted measurement location, the robot maintains its lateral position with its servo control activated, while the MP vertically tracks the sample for vibration isolation. The MP and the robot are described in detail below.

A. Metrology platform (MP)

The MP comprises a rigid mover part equipped with a compact measurement instrument and a mechanical stator part to interface the robot. Figure 2 shows a CAD rendering of the designed platform. For guiding the mover motion in vertical direction and restraining motions in the other degrees of freedom, the mover is suspended by a flexure mechanism consisting of two notch type flexures [18]. For tracking the

sample motion a Lorentz tracking actuator with a motor constant of $K_m = 1.24 \text{ N/A}$ and integrated permanent magnet assembly for passive gravity compensation is used [19]. It is driven by a current-controlled power amplifier, which provides the actuator current i_a . The MP mover mounts an arbitrary compact 3D measurement tool and an on-board tracking sensor (see Fig. 1), based on the laser focus principle, to measure the distance between the MP mover and the target sample surface. The tracking sensor provides a resolution of about 2 nm within a range of $2.5 \mu\text{m}$ and a bandwidth of more than 10 kHz [20].

With the magnets of the actuator and the gravity compensator, the tracking sensor, a dummy mass for a compact measurement tool and the rigid aluminium made mover structure, the MP mover has a resulting mass of $m_p = 4.3 \text{ kg}$. The resulting suspension mode should be as low as possible in order to minimize the transmission of vibrations from the robot carriage to the MP mover [21], such that the flexures are designed to result in a suspension mode at 5 Hz.

B. Gantry robot

The gantry robot uses three linear motors guided by roller bearings (one for the x axis and two for the y axis) to laterally move the carriage in x - and y -direction. The servo control is realized by one PID controller for the x and y axis, respectively, which are implemented on two microprocessor boards (STM32F407G, STMicroelectronics, Switzerland). To prevent limit cycling due to the static friction in the bearings and the integral control, a tolerance band is defined within which the integral action is inactive. The resulting positioning uncertainty is within 400 nm for both axes.

The implemented experimental setup is depicted in Fig. 3a. It shows the gantry robot for lateral positioning, the MP for vertical positioning as well as the sample frame and sample holder, which are directly placed on the workspace floor. Next to the sample mount, a mirror is mounted as target for the on-board tracking sensor in order to enable positioning with nanometer resolution.

III. SYSTEM ANALYSIS

A. System modeling

The lumped mass model of the entire system is depicted in Fig. 3b. The MP mover with mass m_p is actuated by the actuation force F_a , generated via the actuator current i_a , and is connected to the robot carriage via the flexures, modeled by the spring k and the damper d . The additional springs and dampers in Fig. 3b represent the limited stiffness of the robot (k_R and d_R) and the sample frame (k_S and d_S), which result in parasitic relative motion and additional mechanical dynamics. The variables z_{mp} , z_s , and z_r denote the position of the MP mover, the sample, and the robot carriage, respectively. The relative distance between mover and sample $z = z_{mp} - z_s$, which is measured by the tracking sensor, is considered as the plant output, while the actuator current i_a is considered as the control input of the plant. Under the assumption that k and d are sufficiently small and result in a lowly damped suspension mode at low frequencies significantly lower than the targeted

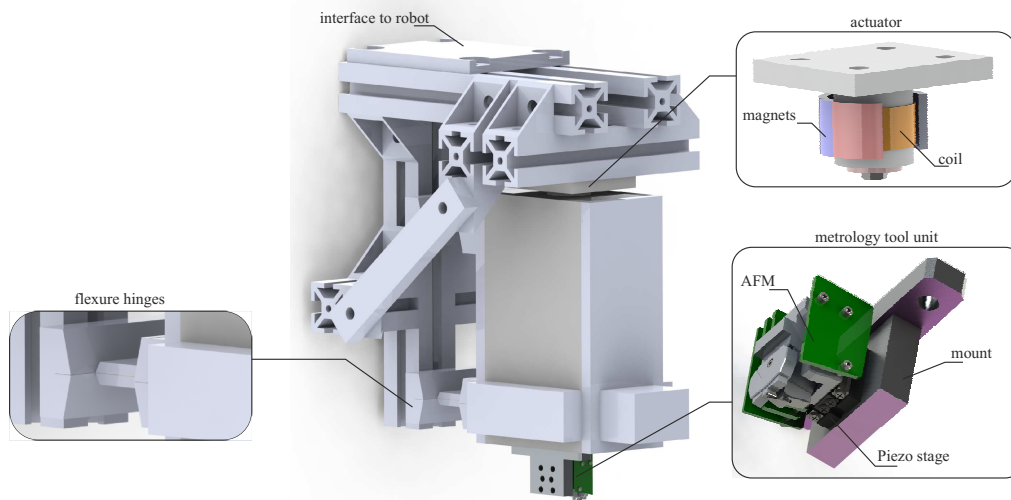


Fig. 2. CAD rendering of the metrology platform (MP). The MP mover is vertically guided by flexure hinges and actuated by a Lorenz actuator with integrated passive gravity compensator. A laser focus sensor measures the relative distance to the sample. A compact AFM is depicted as exemplary measurement tool.

crossover frequency, the plant model $P(s) = z(s)/i_a(s)$ is given by [22]

$$P(s) = P_m(s) \prod_{j=1}^2 \frac{\omega_j}{s + \omega_j} \cdot e^{T_s s}, \quad (1)$$

$$P_m(s) = \frac{G_p}{s^2} \prod_{i=1}^n \left(\frac{\omega_{s,i}^2}{s^2 + 2\zeta_i \omega_{s,i} s + \omega_{s,i}^2} \right)^{p_i}. \quad (2)$$

where $P_m(s)$ represents the mechanical dynamics, G_p is the plant gain, n denotes the number of the modeled modes, and $\omega_{s,i}$ and ζ_i specify the frequency and the damping ratio of each mode, respectively. The parameter p_i determines if the respective term represents a second order pole or zero. The dynamics of the current amplifier and the tracking sensor are modeled individually by a first-order low-pass filter. The parameter $T_s = 50 \mu\text{s}$ is used to consider the delay of the rapid prototyping system used for control implementation, which is running at a sampling frequency of $f_s = 20 \text{ kHz}$.

B. Closed-loop system identification

To experimentally identify the parameters of the derived model, a system identification is performed in a closed-loop configuration. This is necessary to keep the MP mover position within the measurement range of the tracking sensor ($2.5 \mu\text{m}$) by canceling e.g. floor vibrations or thermal drift. A tamed PID controller $C_{pid}(s)$ is selected and parametrized as follows:

$$C_{pid}(s) = K_p + \frac{K_i}{s} + \frac{K_d s}{1 + K_t s}, \quad (3)$$

with K_i denoting the integral gain, K_p the proportional gain and K_d the derivative gain. K_t is used to terminate the derivative action at higher frequencies. For a crossover

frequency ω_c on the mass line, the control gains are calculated by [23]

$$K_i = \tilde{m} (\omega_c / \gamma)^3, \quad (4)$$

$$K_p = \tilde{m} \omega_c^2 / \gamma, \quad (5)$$

$$K_d = \tilde{m} \omega_c, \quad (6)$$

$$K_t = 1 / (\omega_c \gamma), \quad (7)$$

with $\tilde{m} = m_p / K_m$ incorporating the motor constant. The parameter γ defines the stop frequency of the integrator and the bandwidth of the derivative action. $\gamma = 3$ is typically chosen to achieve a good compromise between robustness and performance [23].

The complementary sensitivity function $T_{r,z}(s)$ from the reference r to output z is given by

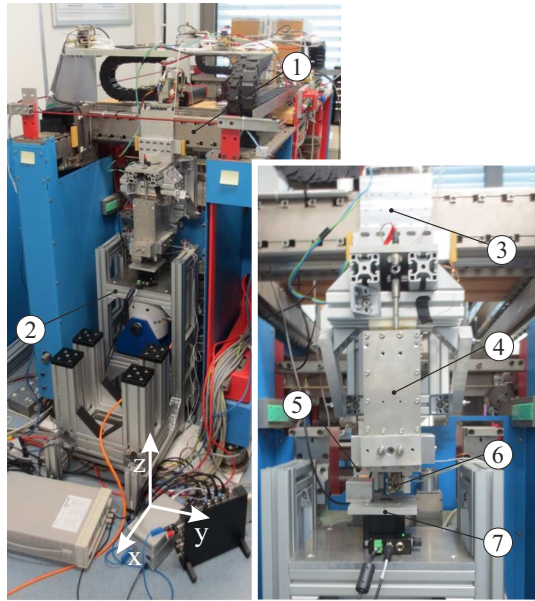
$$T_{r,z}(s) = \frac{C_{pid}(s)P(s)}{1 + C_{pid}(s)P(s)}. \quad (8)$$

As the controller is essentially a constant gain at frequencies higher than $\omega_c \gamma$ due to the tamed derivative action, the second term in the denominator, which is the loop gain, decreases quickly and can be neglected with respect to 1 for higher frequencies, such that $T_{r,z}(s)$ at those frequencies can be approximated by

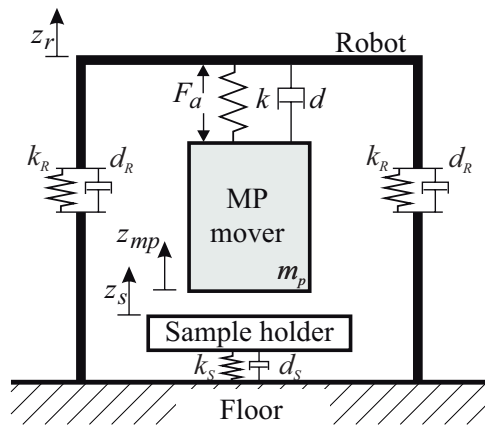
$$T_{r,z}(s) \approx C_{pid}(s)P(s) \approx (K_p + K_d/K_t)P(s). \quad (9)$$

This means that the plant dynamics $P(s)$ can be directly obtained from $T_{r,z}(s)$ under consideration of the constant gain $K_p + K_d/K_t$ of the controller within that frequency range. The crossover frequency ω_c is a tuning parameter which depends on the purpose of the control and is set to $\omega_c = 60 \text{ Hz}$ for identifying the plant dynamics above 200 Hz .

Figure 4 depicts the measured Bode plot of $T_{r,z}(s)$. With the constant control gain at frequencies larger than $\omega_c \gamma = 180 \text{ Hz}$



(a)



(b)

Fig. 3. Robot with metrology platform. (a) shows the setup with (1) xy-positioning bridge of the robot, (2) sample frame, (3) robot carriage, (4) MP mover, (5) tracking sensor, (6) measurement tool mount and (7) sample holder. (b) depicts a lumped mass model with k , d , and F_a representing the stiffness and the damping of the flexure mechanism and the actuation force, respectively.

and the low-pass characteristics of the sensor and the power amplifier, $P(s)$ is estimated by manually fitting the mass-line in a first step. In the second step, the structural modes at frequencies higher than 2 kHz are modeled by manual fitting. The identified parameter values of $P(s)$ with the plant gain $G_p = 0.21$ are given in Table I.

C. Vibration analysis

To maintain a constant distance between the MP mover and the sample, the feedback controller needs to compensate relative vertical motions, which are introduced by vibrations

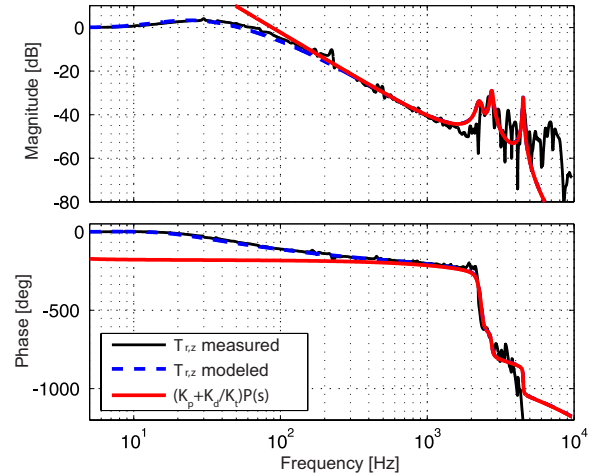


Fig. 4. Measured (solid black line) and estimated (dashed blue line) closed-loop transfer function $T_{r,z}$. The plant model $P(s)$ is fit to $T_{r,z}$ at higher frequencies.

TABLE I
 ESTIMATED PARAMETERS OF PLANT MODEL $P(s)$.

i	ζ_i	$\omega_{s,i}$ [rad/s]	p_i	j	ω_j [rad/s]
1	0.030	$2250 \cdot 2\pi$	1	1	$5500 \cdot 2\pi$
2	0.090	$-2350 \cdot 2\pi$	-1	2	$11000 \cdot 2\pi$
3	0.020	$2750 \cdot 2\pi$	1		
4	0.003	$4500 \cdot 2\pi$	1		

of the robot (z_r) and the sample (z_s). To investigate these vibrations, the MP mover is stabilized by $C_{pid}(s)$, such that it stays within the measurement range of the tracking sensor. For this purpose the feedback controller is redesigned for a lower crossover frequency $\omega_c = 30$ Hz, such that the tracking error components above 30 Hz can essentially be considered the vibration characteristics of interest. To distinguish the individual vibration sources, the vibrations in the system are investigated for the cases with (i) deactivated and (ii) activated lateral motion control of the robot. Figure 5 shows the time signal, the power spectral density (PSD), and the corresponding cumulative power spectral density (CPSD) of the measured tracking error for both cases.

Case 1: With deactivated robot motion control, the tracking error is 58 nm(rms), with significant components up to 50 Hz according to the CPSD. However, the lateral position of the robot carriage deviates from the desired position due to the cogging forces of the linear motor. To maintain the desired lateral position, motion control for the robot thus needs to be activated.

Case 2: With the lateral position of the robot carriage actively regulated by the robot controllers, the tracking error increases to 83 nm(rms). The CPSD reveals that the increase is mainly due to vibration components at 100 Hz and 150 Hz, which are higher harmonics of the 50 Hz vibrations visible in the PSD. This is most likely due to noise coupling from the robot power supply, which results in vibrations of the robot carriage and an increased variation of the distance between

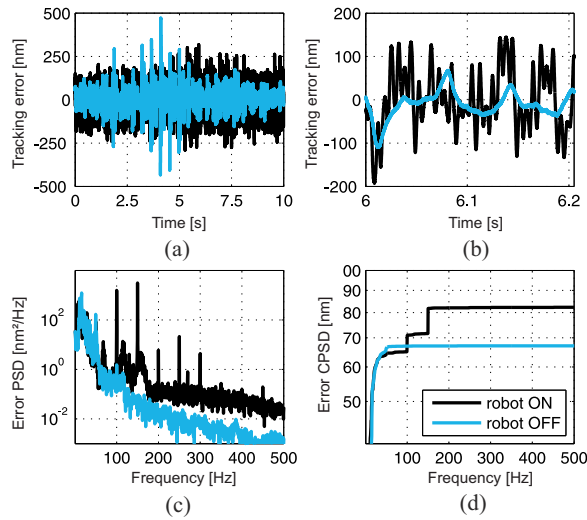


Fig. 5. Tracking error measured in closed-loop with a control bandwidth of about 30 Hz when the robot controller turned off (blue) and on (black): (a) time signal, (b) zoomed time signal, (c) PSD, and (d) corresponding CPSD.

the MP mover and the sample.

IV. HIGH PERFORMANCE TRACKING CONTROLLER DESIGN

In order to investigate the achievable performance of the MP with the robot, this section presents the motion control design based on the analysis in Sec. III. Being aware of advanced concepts for disturbance rejection such as ARC [24] or ADRC [25], a model-based PID controller design approach is used due to the simplicity of the designed plant and the non-varying harmonic disturbances. A high control bandwidth is targeted in order to reject broad-band vibrations and supplemental peak filters are added in order to improve the rejection performance at the vibration peaks at 100 Hz and 150 Hz, obtained in the previous section. The resulting controllers are discretized by pole-zero matching [26] for implementation on the rapid prototyping system (Type: DS1202, dSPACE GmbH, Germany) running at a sampling frequency of 20 kHz.

A. PID Controller with notch filters

As depicted in Fig. 4, the mechanical plant shows parasitic structural dynamics beyond 2 kHz, which influence the achievable control bandwidth. In order to compensate them, the PID controller designed according to (3) is cascaded with notch filters [27]

$$C_m(s) = C_{pid}(s) \prod_{i=1}^2 \frac{s^2 + 2\zeta_{n,i}\eta_{n,i}\omega_{n,i}s + \omega_{n,i}}{s^2 + 2\zeta_{n,i}\omega_{n,i}s + \omega_{n,i}}, \quad (10)$$

where $\omega_{n,i}$, $\zeta_{n,i}$, and $\eta_{n,i}$ denote the frequency, the width, and the depth of the notch, respectively. Two notch filters are implemented to compensate for the resonances around 2.5 kHz and 4.5 kHz with the parameter values given in Table II. Designing $C_{pid}(s)$ with a model-based loop shaping approach

[23] for an open-loop crossover frequency of 270 Hz, results in a phase margin of 30° and controller gains of $K_i = 1.38e4$, $K_p = 5.64$, $K_d = 7.7e-3$, and $K_t = 1.52e-4$. Figure 9 shows a Bode plot of the resulting controller $C_m(s)$.

TABLE II
PARAMETERS OF THE NOTCH FILTERS OF $C_m(s)$.

i	$\eta_{n,i}$	$\zeta_{n,i}$	$\omega_{n,i}$ [rad/s]
1	0.05	0.2	$2550 \cdot 2\pi$
2	0.1	0.5	$5000 \cdot 2\pi$

B. Peak filter design

As revealed in Sec. III-C, the robot introduces narrow-band vibrations at 100 Hz and 150 Hz, which are most likely caused by noise coupling from the robot power supply and increase the distance variation between MP and sample (see Fig. 5(d)). The control gain of $C_m(s)$ is, however, relatively low around these frequencies (see Fig. 9), such that the disturbance rejection of these harmonic vibrations is fairly limited.

To reject harmonic vibrations, compensation methods such as adaptive repetitive control [28], [29] and adaptive feed-forward cancellation [30] are reported. Both compensation techniques exhibit a similar control structure and rely on determining the disturbances to find proper control gains that decrease the gain of the sensitivity function at the harmonic frequencies. Adaptive and learning laws are often applied to make them robust with respect to varying disturbances and model uncertainties, leading to complex and computationally intensive control structures. Another approach is the application of resonant filters to implement high gain controllers [31], [32].

To efficiently reject the harmonic vibrations at 100 Hz and 150 Hz, resonant filters are implemented by peak filters. The peak filters are cascaded to $C_m(s)$, such that the entire controller dynamics are obtained by logarithmically adding the gain and phase characteristics of the peak filters and $C_m(s)$. A peak filter $C_{pf}(s)$ is given by

$$C_{pf}(s) = \frac{s^2 + 2(-1)^k \zeta_p \omega_p s + \omega_p^2}{s^2 + 2\frac{\zeta_p}{d_p} \omega_p s + \omega_p^2}, \quad (11)$$

with ω_p denoting the peak frequency. The parameters d_p and ζ_p are related to the height and width of the peak, respectively. The parameter $k = \{1, 2\}$ specifies the location of the zero in either the right half (RHP) or in the left half (LHP) of the Laplace plane. In Fig. 6 the simulated gain and phase responses of $C_{pf}(s)$ are shown for $d_p = 10$, the configurations with a RHP and a LHP zeros and varying values of ζ_p . The gain response is symmetric while the phase response is asymmetric about the peak frequency. A pair of LHP zeros results in an increasing phase lead followed by a decreasing phase lag as the frequency increases. A pair of RHP zeros results in an increasing phase lag starting from 0° at low frequencies and ending at -360° at frequencies sufficiently higher than ω_p .

The impact of a peak filter on the closed-loop system stability is analyzed by the Nyquist plot of the open-loop

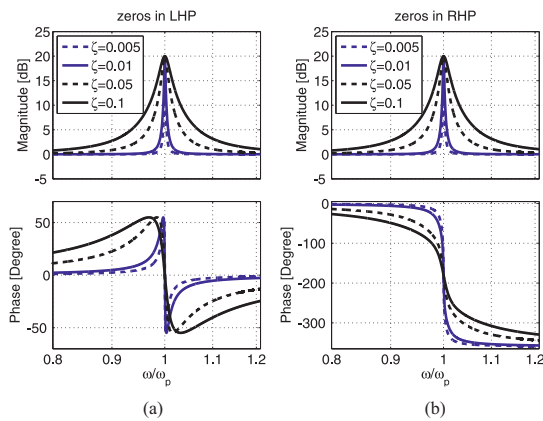


Fig. 6. Frequency response of peak filters for different values of ζ_d . The placement of the zeros in (a) the LHP and (b) the RHP results in the same gain responses but different phase responses.

transfer function $L_{ez}(s) = C_{pid}(s)C_{pf}(s)P(s)$. Higher order dynamics of the plant $P(s)$ are neglected in this analysis as they are compensated by the notch filters of $C_m(s)$. Figure 7 shows the Nyquist plots of $L_{ez}(s)$ for varying values of ω_p ($d_p = 10$ and $\zeta_p = 0.005$) for the case of LHP zeros and RHP zeros:

- With $C_{pf}(s)$ having zeros in the LHP (see Fig. 7 (a)), $L_{ez}(s)$ shows an additional counterclockwise circle with its center towards the negative real axis, approaching the -1 Nyquist point with increasing ω_p . To maintain stability, the -1 Nyquist point has to be outside the encircled area, thus specifying an upper limit on ω_p .
- With $C_{pf}(s)$ having zeros in the RHP (see Fig. 7 (b)), the center of the caused additional circle is shifted towards the positive real axis. Notice that the smaller ω_p is, the smaller the vector margin gets, creating the lower limit of ω_p .

In summary, a peak filter with the zeros in the LHP can be used to compensate harmonic disturbances with frequencies below or slightly above ω_c , while peak filters with the zeros in the RHP are exclusively for harmonic disturbances significantly above ω_c .

C. Peak filter analysis

While peak filters improve the disturbance rejection at the specified frequencies, they amplify the disturbances at other frequencies due to Bode's sensitivity integral. To analyze the impact of the peak filter on the disturbance rejection, the ratio δS between the sensitivity function without peak filter $S_{np}(s)$ and with peak filter $S_{wp}(s)$ is introduced as

$$S_{np}(s) = 1/(1 + C_m(s)P(s)), \quad (12)$$

$$S_{wp}(s) = 1/(1 + C_m(s)C_{pf}(s)P(s)), \quad (13)$$

$$|\delta S| := \left| \frac{S_{wp}(s)}{S_{np}(s)} \right| = \left| \frac{1 + C_m(s)P(s)}{1 + C_m(s)C_{pf}(s)P(s)} \right|. \quad (14)$$

The ratio δS is shown for varying values of ω_p with respect to ω_c in Fig. 8. It is clearly visible that the peak filter

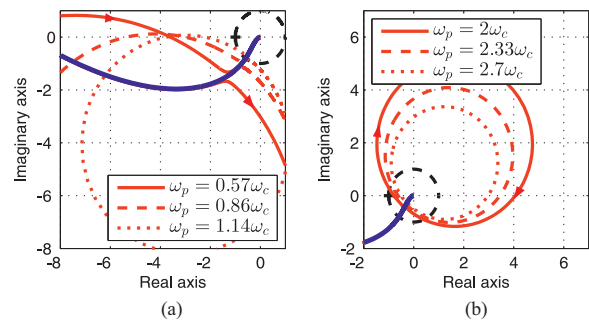


Fig. 7. Nyquist plots of the open-loop transfer function $L_{ez}(s)$ (only positive frequencies are shown). The second order plant with the PID controller is depicted in blue. The loop gains with the PID controller and peak filters at various frequencies ω_p and zeros in (a) the LHP or (b) the RHP are depicted in red. The system is stable as long as the -1 point is not encircled.

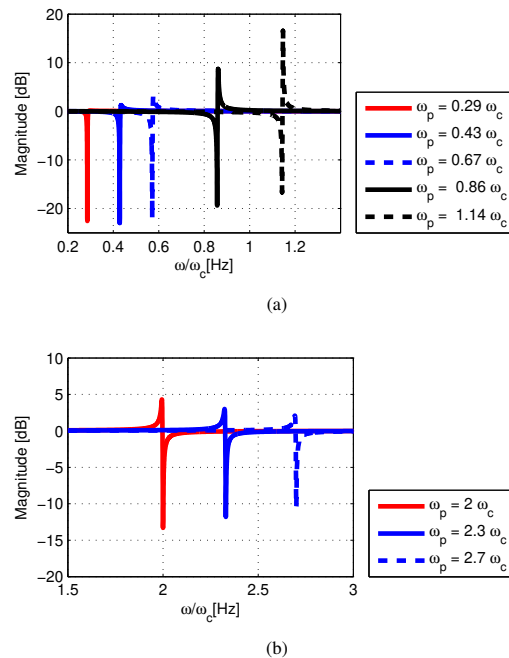


Fig. 8. Magnitude of the sensitivity functions ratio δS with peak filters for (a) the zeros in LHP ($k = 1$) and (b) the zeros in RHP ($k = 2$).

not only improves the disturbance rejection at ω_p , but also amplifies disturbances in the vicinity of ω_p . Depending on the peak filter implementation, this amplification takes place above (for $k = 1$) or below ω_p (for $k = 2$). The smaller the difference $|\omega_c - \omega_p|$, the higher the peak gain of the sensitivity function around ω_p . Overall, the disturbance rejection at ω_p is significantly improved, but the additional amplification of disturbances such as vibrations or sensor noise close to ω_p has to be considered in order to prevent the overall tracking error from increasing.

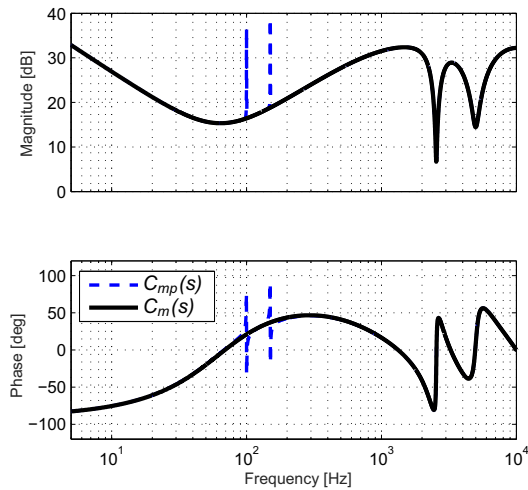


Fig. 9. Frequency response of the designed controllers $C_m(s)$ and $C_{mp}(s)$. The peak filters locally increase the controller gain of $C_{mp}(s)$ by approximately 20 dB.

D. Determination of peak filter parameters

Peak filters are implemented for the harmonic vibrations occurring at 100 Hz and 150 Hz. As these harmonics are well below $f_c = 270$ Hz, two peak filters with $k = 1$ are selected to maintain stability. The parameters of the peak filters are listed in Tab. III. The entire feedback controller consisting of the PID controller with the notch filters and the two peak filters is given by

$$C_{mp}(s) = C_m(s) \prod_{i=1}^2 C_{pf,i}(s). \quad (15)$$

As shown in Fig. 9, the gain of $C_{mp}(s)$ is successfully increased by about a factor of 10 at the desired frequencies, with respect to $C_m(s)$.

TABLE III
 PARAMETERS OF THE PEAK FILTERS $C_{pf,i}(s)$.

i	$d_{p,i}$	k	$\zeta_{p,i}$	$\omega_{p,i}$ [rad/s]
1	10	2	0.005	$100 \cdot 2\pi$
2	10	2	0.005	$150 \cdot 2\pi$

V. EXPERIMENTS

A. Experimental design

In order to validate the disturbance rejection capability of the system designed in Section II together with the controllers designed in Section IV the tracking error is evaluated in the frequency and time domain. For this purpose the designed controllers C_m and C_{mp} are implemented on a rapid prototyping system (Type: DS1202, dSPACE GmbH, Germany). The sensitivity function, as measure for the disturbance rejection in the frequency domain and given by $S(s) = 1/(1+C(s)P(s))$,

is acquired by using a system analyzer (3562 A, Hewlett-Packard, Palo Alto, CA, USA) to measure the frequency response from system input to error signal. For evaluating the error in the time domain, the resulting output of the tracking sensor in closed-loop control with each of the two controllers is measured with activated lateral motion control of the robot (see Section III-C).

B. Experimental results

The measured sensitivity function is depicted in Fig. 10(a) and shows good accordance with the simulated response, validating the previous modeling. The control bandwidth (the unity-gain crossover frequency) is 180 Hz. More importantly, the influence of the peak filters is clearly visible by comparing the measured response with $C_{mp}(s)$ and the simulated response with $C_m(s)$. The peak filters successfully enhance the disturbance rejection at 100 Hz and 150 Hz by about 20 dB, equalling a factor of 10, which is determined by the peak height $d_{p,i}$ in the peak filters' design.

Figure 10(b) shows the measured tracking error, i.e. the deviation from the constant setpoint value 0, in the time and frequency domain. The feedback controller without the peak filters $C_m(s)$ results in a tracking error of 28 nm(rms). Evaluation of the PSD and the CPSD of the tracking error shows good vibration rejection below 100 Hz. It is also visible that the harmonic vibrations at 100 Hz and 150 Hz result in a tracking error of about 20 nm(rms). With the peak filters, $C_{mp}(s)$ significantly decreases the harmonic vibrations at 100 Hz and 150 Hz, as shown by the PSD and CPSD. The resulting overall tracking error is 15 nm(rms), which is another decrease by a factor of 2 as compared to the initial PID controller and only 18% of of the vibrations in the workspace, which were measured in Sec. III-C.

In summary it is shown that the designed MP as endeffector enables high precision positioning for robot-based inline metrology applications and that the proposed peak filter design can locally improve the rejection of harmonic vibrations of the robot, resulting in an overall 82% reduction of the present vibrations and a small remaining tracking error of only 15 nm.

VI. CONCLUSION

For enabling high precision measurements directly in a vibration prone production line, a metrology platform is designed as robotic endeffector, with its mover vertically tracking the sample to be evaluated. In order to reject broad-band floor vibrations for precise tracking control, a PID feedback controller is designed based on a loop shaping approach, employing notch filters to cancel parasitic mechanical dynamics of the robot structure. A vibration analysis shows that the active servo control of the robot introduces additional vibrations with narrow-band frequency spectra at 100 Hz and 150 Hz. To handle these narrow-band disturbances and to improve the disturbance rejection capability, a method for designing supplemental peak filters is introduced, which succeed the PID controller and are tailored to the disturbance criteria by locally increasing the loop gain. The experiments demonstrate the effectiveness of the system design in combination with

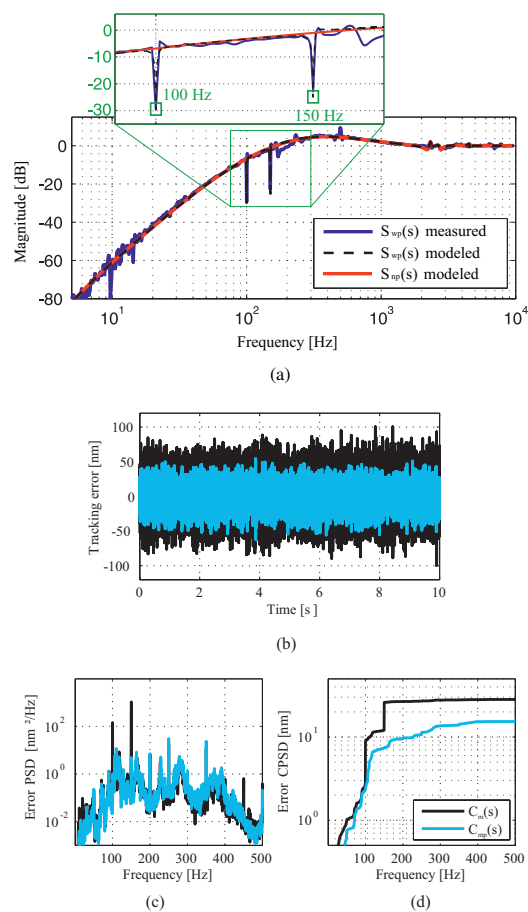


Fig. 10. Performance evaluation in the frequency and time domain. (a) Measured and simulated sensitivity functions with the peak filters enhancing the disturbance rejection by a factor of 10 at 100 Hz and 150 Hz. (b) Measured tracking error in the time domain, (c) the error spectrum and (d) the cumulative power spectrum density with $C_{mp}(s)$ and $C_m(s)$.

the designed controller and the supplemental peak filters by significantly decreasing the tracking error to 15 nm(rms), enabling high resolution inline measurements.

ACKNOWLEDGMENT

The financial support by the Christian Doppler Research Association, the Austrian Federal Ministry for Digital and Economic Affairs, and the National Foundation for Research, Technology and Development, as well as MICRO-EPSILON MESSTECHNIK GmbH & Co. KG and ATENSOR Engineering and Technology Systems GmbH, as well as by the European 7th Framework Programme (no. 309558) is gratefully acknowledged.

REFERENCES

[1] R. Schmitt and F. Moening, "Ensure success with inline-metrology," in *IMEKO XVIII World Congress*, 2006.

[2] H. A. Ching, D. Choudhury, M. J. Nine, and N. A. A. Osman, "Effects of surface coating on reducing friction and wear of orthopaedic implants," *Science and Technology of Advanced Materials*, vol. 15, p. 014402, 2014.

[3] S. Chen, C. Cheung, C. Zhao, and F. Zhang, "Simulated and measured surface roughness in high-speed grinding of silicon carbide wafers," *The International Journal of Advanced Manufacturing Technology*, vol. 91, no. 1, pp. 719–730, Jul 2017.

[4] P. Eaton and P. West, *Atomic Force Microscopy*. Oxford University Press, 2010.

[5] R. Leach, *Fundamental Principles of Engineering Nanometrology*. Elsevier Science & Technology, 2014.

[6] S. Ito, M. Poik, E. Csencsics, J. Schlarp, and G. Schitter, "High-speed scanning chromatic confocal sensor for 3-d imaging with modeling-free learning control," *Applied Optics*, vol. 59, no. 29, pp. 9234–9242, 2020.

[7] H. Amick, M. Gendreau, T. Busch, and C. Gordon, "Evolving criteria for research facilities I: vibration," in *Proc. SPIE 5933*, vol. 5933, 2005, p. 593303.

[8] R. Munnig Schmidt, G. Schitter, A. Rankers, and J. van Eijk, *The Design of High Performance Mechatronics*, 2nd ed. Delft University Press, 2014.

[9] M. Beijen, M. Heertjes, J. V. Dijk, and W. Hakvoort, "Self-tuning MIMO disturbance feedforward control for active hard-mounted vibration isolators," *Control Engineering Practice*, vol. 72, pp. 90 – 103, 2018.

[10] J. Rejc, J. Cinkelj, and M. Muni, "Dimensional measurements of a gray-iron object using a robot and a laser displacement sensor," *Robotics and Computer-Integrated Manufacturing*, vol. 25, no. 1, pp. 166–167, 2009.

[11] I. Iglesias, M. Sebastian, and J. Ares, "Overview of the state of robotic machining: Current situation and future potential," *Procedia Engineering*, vol. 152, pp. 911–917, 2015.

[12] U. Schneider, M. Drust, M. Ansaloni, C. Lehmann, M. Pellicciari, F. Leali, J. W. Gunnink, and A. Verl, "Improving robotic machining accuracy through experimental error investigation and modular compensation," *The International Journal of Advanced Manufacturing Technology*, vol. 85, no. 1, pp. 3–15, Jul 2016.

[13] S. Ito, S. Unger, and G. Schitter, "Vibration isolator carrying atomic force microscope's head," *Mechatronics*, vol. 44, pp. 32 – 41, 2017.

[14] R. Saathof, M. Thier, R. Hainisch, and G. Schitter, "Integrated system and control design of a one DoF nano-metrology platform," *Mechatronics*, vol. 47, pp. 88 – 96, 2017.

[15] S. Ito and G. Schitter, "Atomic force microscopy capable of vibration isolation with low-stiffness z-axis actuation," *Ultramicroscopy*, vol. 186, pp. 9 – 17, 2018.

[16] G. Schitter and A. Stemmer, "Eliminating mechanical perturbations in scanning probe microscopy," *Nanotechnology*, vol. 13, no. 5, pp. 663–665, 2002.

[17] M. Thier, R. Saathof, E. Csencsics, R. Hainisch, A. Sinn, and G. Schitter, "Design and control of a positioning system for robot-based nanometrology," *at - Automatisierungstechnik*, vol. 63, no. 9, pp. 727–738, sep 2015.

[18] L. Howell, S. Magleby, and B. Olsen, *Handbook of Compliant Mechanisms*. John Wiley & Sons, 2013.

[19] R. Deng, R. Saathof, J. Spronck, S. Hol, and R. Munnig Schmidt, "Integrated 6-dof lorentz actuator with gravity compensator for precision positioning," *22nd International conference on magnetically levitated systems and linear drives*, 2014.

[20] D. Dontsov and W. Schott, "Heterodyne interferometer for in-plane vibration and displacement measurements," *Industrial Technologies 2016, Amsterdam, The Netherlands*, 2016.

[21] S. Ito and G. Schitter, "Comparison and classification of high-precision actuators based on stiffness influencing vibration isolation," *IEEE/ASME Transactions on Mechatronics*, vol. 21, no. 2, pp. 1169–1178, April 2016.

[22] A. Preumont, *Vibration control of active structures*, 3rd ed. Dordrecht: Kluwer academic publishers, 2011.

[23] E. Csencsics and G. Schitter, "Parametric pid controller tuning for a fast steering mirror," *IEEE Conference on Control Technology and Applications*, pp. 1673–1678, 2017.

[24] B. Yao, M. Al-Majed, and M. Tomizuka, "High-performance robust motion control of machine tools: An adaptive robust control approach and comparative experiments," *IEEE/ASME Transactions on Mechatronics*, vol. 2, no. 2, pp. 63–76, 1997.

[25] J. Han, "From pid to active disturbance rejection control," *IEEE Transactions on Industrial Electronics*, vol. 56, no. 3, pp. 900–906, 2009.

[26] G. Franklin, D. Powell, and M. Workman, *Digital Control of Dynamic Systems*. Prentice Hall, 1997.

- [27] T. Yamaguchi M. Hirata and C. Pang, *High-Speed Precision Motion Control*. Taylor & Francis, 2011.
- [28] N. Perez-Arancibia, T.-C. Tsao, and J. Gibson, "A new method for synthesizing multiple-period adaptive repetitive controllers and its application to the control of hard disk drives," *Automatica*, vol. 46, no. 7, pp. 1186 – 1195, 2010.
- [29] E. Kurniawan, Z. Cao, and Z. Man, "Adaptive repetitive control of system subject to periodic disturbance with time-varying frequency," *2011 First International Conference on Informatics and Computational Intelligence*, pp. 185–190, 2011.
- [30] S. Yabui and I. Kajiwara, "A comparison study between a resonant filter and an adaptive feed-forward cancellation for implementation of a control system," *IEEE 13th International Workshop on Advanced Motion Control*, pp. 598–603, 2014.
- [31] T. Atsumi, A. Okuyama, and M. Kobayashi, "Track-following control using resonant filter in hard disk drives," *IEEE/ASME Transactions on Mechatronics*, vol. 12, no. 4, pp. 472–479, Aug 2007.
- [32] E. Csencsics and G. Schitter, "System design and control of a resonant fast steering mirror for lissajous-based scanning," *IEEE/ASME Transactions on Mechatronics*, vol. 22, no. 5, pp. 1963–1972, 2017.



Georg Schitter is Professor for Advanced Mechatronic Systems at the Automation and Control Institute (ACIN) of TU Wien. He received an MSc in Electrical Engineering from TU Graz, Austria (2000) and an MSc and PhD degree from ETH Zurich, Switzerland (2004). His primary research interests are on high-performance mechatronic systems, particularly for applications in the high-tech industry, scientific instrumentation, and mechatronic imaging systems, such as AFM, scanning laser and LIDAR systems, telescope systems, adaptive optics, and lithography systems for semiconductor industry.

He received the journal best paper award of IEEE/ASME Transactions on Mechatronics (2018), of the IFAC Mechatronics (2008-2010), of the Asian Journal of Control (2004-2005), and the 2013 IFAC Mechatronics Young Researcher Award. He served as an Associate Editor for IFAC Mechatronics, Control Engineering Practice, and for the IEEE Transactions on Mechatronics.



Ernst Csencsics Ernst Csencsics is postdoctoral researcher in the Advanced Mechatronic Systems Group at the Automation and Control Institute (ACIN) of TU Wien. He received an MSc. and a PhD degree in Electrical Engineering from TU Vienna, Austria in 2014 and 2017, respectively. His primary research interests are on high performance mechatronic systems, the development of holistic methods for multidisciplinary system design and integration, opto-mechatronic measurement and imaging systems, precision engineering, and robot-based

in-line measurement systems.

He received the journal best paper award of IEEE/ASME Transactions on Mechatronics (2018) and the best student paper award at the American Control Conference (2016).



Markus Thier was a PhD student at the Automation and Control Institute (ACIN) at Vienna University of Technology. He received an MSc. degree in Electrical Engineering from TU Vienna, Austria in 2012. His primary research interests were on mechatronic systems design, precision engineering and vibration isolation for in-line metrology, real time systems for signal processing, and wave front sensing.

He is currently working as a system design engineer for electrical motors at Magna Powertrain.



Shingo Ito received the MASc in Mechanical and Industrial Engineering from the University of Toronto, Canada, in 2007 and the PhD in Electrical Engineering from TU Wien, Vienna, Austria in 2015. From 2007 to 2010, he served as an engineer in the field of motion control at Yaskawa Electric Corporation, Japan, and worked as researcher and postdoc in the Advanced Mechatronic Systems Group at the ACIN of TU Wien from 2011 to 2021.

He is currently associate professor at the Faculty of Engineering of the University of Fukui, Japan. His research interest includes design and control of high-precision mechatronic systems for production, inspection and automation.